ALTERNATE: Experimental and modeling study of soot formation in high-pressure kerosene and SAF combustion

Cornelia Irimiea, Axel Vincent-Randonnier, Jean Pierre Dufitumukiza, Stefano Puggelli, Jean-Baptiste May-Carle, Nicholas Treleaven, Thomas Lesaffre, Alexandre Coudray, Etienne Lameloise, Bénédicte Cuenot, et al.

ALTERNATE: Experimental and modeling study of soot formation in high-pressure kerosene and SAF combustion

Cornelia IRIMIEA[3], Axel VINCENT-RANDONNIER[3], Jean Pierre DUFITUMUKIZA[3,4], Stefano PUGGELLI[1], Jean-Baptiste MAY-CARLE[1], Nicholas TRELEAVEN[1], Thomas LESAFFRE[2], Alexandre COUDRAY[2], Etienne LAMELOISE[2], Bénédicte CUENOT[2], Eleonore RIBER[2], Nicolas FDIDA[3], Pascal CHERUBINI[3], Xavier MERCIER[4]

[1]Safran Tech, Rue des Jeunes Bois, Châteaufort, 78114 Magny-les-Hameaux, France; [2]CERFACS, 42 Avenue Gaspard Coriolis, 31057 Toulouse, France; [3]ONERA, 6 chemin de la vauve aux Granges, 91123, Palaiseau, France; [4]Lille Univ., CNRS, PC2A, Villeneuve d'Ascq, 59655, France

*Corresponding author email: jean-baptiste.may-carle@safrangroup.com

Abstract

The EU-funded project ALTERNATE aims to explore the possibility of broader use of sustainable aviation fuels (SAFs). Part of the project assesses the effect of SAFs on soot production using experimental results and model predictions. In this regard, the combustion of two fuels was investigated under high-pressure conditions on the MICADO test rig at ONERA. This combustor allows a detailed analysis of soot formation based on advanced laser diagnostics. During the experimental campaign, the effect of Jet A-1 and Alcohol to Jet (ATJ) on soot levels was studied for three operating conditions in which the pressure of the combustion chamber varied from 4.5 to 9 bar, while maintaining almost constant the fuel-to-air ratio. An investigation of spray formation, flame shape and combustion dynamics is carried out to shed light on the impact of fuel composition on soot formation. In addition, the sooting behavior of the two fuels is compared, and it is observed that ATJ has a lower sooting capacity than Jet A-1 for the studied conditions. In parallel, Safran Tech and CERFACS worked jointly to perform Large Eddy Simulation (LES) for the case 4.5 bar fueled with Jet A-1. Semi-detailed chemistry for fuel oxidation and gaseous soot precursors together with the Lagrangian Soot Tracking model, both developed by CERFACS, is applied, and a first comparison against the available experimental data in terms of spray evolution and flame shape is obtained. The present work gives an overview of the experimental data collected during ALTERNATE, of SAF effects on soot generation and a first comparison obtained with LES for the Jet A-1 case at 4.5 bar.

Keywords

SAF, combustion, soot, high pressure, optical metrology, modeling, Large Eddy Simulation

Introduction

The aviation industry has to look for renewable energy sources as a short-term solution for reducing gas and particulate emissions due to the stringent standards imposed on emissions and the increasing demand for air traffic [1]. Lately, outstanding progress toward cleaner combustion has been achieved due to the development of lasers and fast acquisition systems and, nonetheless, due to the increased processing power of computers [2, 3]. However, despite these advancements, the characterization and understanding of combustion in industrial-scale combustors and, even more, with sustainable aviation fuels (SAF) is still limited. From an experimental point of view, the coupling of non-intrusive optical techniques, which can provide simultaneous experimental information about the involved physical phenomena (e.g., turbulent flow field, flame, spray, pollutant emissions), is becoming crucial. Implementing extensive optical technique measurements inside aircraft engines is expensive and almost impossible. In this regard, ONERA has dedicated test rig platforms for studying high-pressure and high-temperature combustion conditions similar to those identified in aero-engines. The MICADO

test rig, which consists of a single injector combustor with optical access in the reactive zone, belongs to this group. Optical diagnostics are custom developed for characterizing a highly turbulent environment. Complex phenomena such as the evaporation of the fuel, spray dynamics and pollutants formation are monitored with optical techniques such as Mie and Rayleigh scattering, OH* chemiluminescence and laser induced incandescence (LII) for a matrix of selected fuels and blends.
In order to complement the information obtained from experimental campaigns, Large Eddy Simulation (LES) is nowadays a valuable solution, especially when analyzing industrial configurations. However, an important volume of work for model validation is required to take confidence in the LES results, especially when pollutants are investigated. The present study is a step forward in realizing a joint experimental/numerical investigation on soot generation from Jet A-1 and SAF combustion in high-pressure and high-temperature conditions. This collaboration was possible in the framework of the ALTERNATE project [4], where ONERA, SAFRAN Tech and CERFACS work jointly to combine experimental data and numerical results to understand soot formation and predict soot levels. Three operating conditions (OCs) representative of Taxi, Approach and Cruise LTO cycles were studied with optical techniques when burning Jet A-1 and Alcohol to Jet (ATJ) fuels in similar fuel-to-air ratios (FAR) at ONERA on the MICADO test rig. Employed optical techniques give access to the spray characteristics (scattering techniques), the flame front position (OH* chemiluminescence) and soot distribution (LII). These data provide information about the flame dynamics, fuel evaporation rates, heat release rate and semi-quantitative information about soot between the tested OCs and fuels. In parallel, LES has been carried out by Safran Tech and CERFACS on one OC for Jet A-1 in order to obtain a first comparison with the available experimental data and gain a better insight into soot generation in the present case. The paper is structured as follows: first, the MICADO test rig and the OCs studied experimentally are described, followed by the numerical setup. After that, the attention is directed toward the description of the experimental data collected with Jet A-1 and ATJ and to the comparison with the LES results for Jet A-1 fuel.

MICADO test rig

The MICADO test rig was used to investigate the high-pressure and temperature conditions that characterize aeronautical combustors [5]. This rig comprises the combustor facility, a dedicated optical laboratory placed above the test rig enclosure and a control room. Optical access is obtained thanks to three removable optical port views, i.e., two placed on the sides and one on the bottom of the combustor. Visual access and optical laser diagnostics are possible over a distance of 89 mm from the injector. The combustion chamber is 100 mm × 100 mm tubular square section. The combustor walls are water-cooled, thus allowing continuous running operating conditions for up to two hours after reaching stable conditions. Air and fuel are fed to the combustor through an axial swirl injector able to generate stable aerodynamic conditions. Two injection locations are provided: a main injection that introduces the fuel inside the channel of the swirled air, and a pilot system shown in the sectional side view in Fig. 1. The fuel and the pressure are stabilized with an exit Delavan nozzle and an adjustable throttling plug. The high-pressure airflow (240 - 492 g·s^{-1}) is heated to a temperature of ~550 K with a heat exchanger coupled to a kerosene burner. The inlet air mass flow entering the MICADO combustor is measured with a Venturi tube placed upstream of the injector inlet. Cooling of the optical windows is realized with 29% of the total airflow deviated with a metallic backplate, and the remaining 71% of airflow passed through the swirler (see Fig. 1). A dedicated LABVIEW acquisition platform ensures the operating control of the installation, as well as the temporal monitoring and record of the mass flow rates, the pressure inside the combustor and temperature. Three OCs were selected for this study. Jet A-1 and ATJ combustion was studied independently for each OC. These tests resulted in six individual OCs with specific operating parameters, as summarized in Tab. 1. The lower heating values (LHV) of Jet A-1 and ATJ are 43.21 MJ/kg and 44.06 MJ/kg.

		P_{ch} (MPa)		T_{air} (K)		$\dot{m}_{air}$ (g/s)		$\dot{m}_{fuel}$ (g/s)		Φ	
		Avg	Std	Avg	Std	Avg	Std	Avg	Std	Avg	Std
OC_1	Jet A-1	0.45	3.4×10^{-3}	540.6	0.9	241.3	0.8	13.2	0.02	0.80	3.2×10^{-3}
	ATJ	0.45	2.2×10^{-3}	526	0.4	244	1.4	12.4	0.08	0.77	7.4×10^{-3}
OC_2	Jet A-1	0.79	6.9×10^{-3}	555.6	0.3	491.7	1.3	22.9	0.10	0.68	3.7×10^{-3}
	ATJ	0.79	1.5×10^{-3}	549.6	0.1	491.9	1.0	24.1	0.25	0.72	7.6×10^{-3}
OC_3	Jet A-1	0.94	8.5×10^{-3}	553.3	0.1	347.4	0.9	18.5	0.11	0.78	5×10^{-3}
	ATJ	0.93	1.8×10^{-3}	546.8	0.7	347.2	1.7	18.3	0.10	0.77	5.7×10^{-3}

Table 1. Operating conditions tested during the ALTERNATE project on the MICADO test rig for Jet A-1 and ATJ fuels.

However, due to MICADO system inertia, the global equivalence ratio (Φ) of Jet A-1 and ATJ for the same operating conditions are slightly different. In particular, Φ of Jet A-1 is slightly higher for conditions OC1 and OC3, while for OC2, Φ is superior for ATJ fuel. The fuel was injected in 100% pilot mode for all OCs.

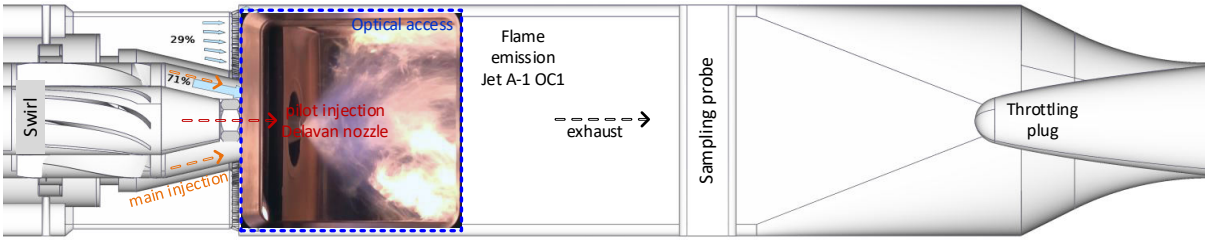

Figure 1. Sectional side view and fluid domain of MICADO test rig. One example of the visible flame emission stabilized in OC1 with Jet A-1 is represented in the optical port view area.

Coupled optical techniques: laser diagnostics and high-speed imaging

Test rig measurement campaigns are extensive and costly, hence the interest in coupling optical techniques for obtaining many parameters of importance during one OC. Two lasers and four cameras were used to build a coupled system to measure the chemiluminescent emission of hydroxyl radical (OH*), scattering from unburned fuel and soot particles, and laser induced incandescence (LII) signal from soot. All necessary instrumentation used for the in-situ optical techniques was placed around the MICADO test rig. The laser beams were directed in the test rig enclosure through two ports dedicated to the optical access from the laboratory to the test rig room. The laser beams were converted into two laser sheets, superimposed at the horizontal axial plane of the combustor with coupling laser line mirrors. The two laser sheets were aligned with the injector nozzle while covering a region of interest of 100 mm in length and 89 mm in height. The focal point of the laser sheet generator lenses was aligned with the injector nozzle. Flame emission and induced signals were directed toward three dichroic mirrors via a UV-visible, highly reflective mirror placed below the combustor. Each camera was equipped with a dedicated filter. Data acquisition was remotely performed from the control room and synchronized with the operation of the test rig. A first dichroic mirror reflected the UV emission toward an intensified relay optics (IRO) module coupled with a Phantom V710 camera used to record the chemiluminescence of OH* at 10 kHz during 4 µs gate width (GW). This camera had 94 mm focal length CERCO UV lenses set at f4 aperture. The lenses were equipped with a short bandpass filter with a bandwidth of 10 nm centered at 310 nm. Scattering induced with 527 nm at 10 kHz was recorded simultaneously with OH* by a second Phantom V711 camera during a GW of 0.3 µs. The camera was equipped with 135 mm (F/8) lenses and a narrow-bandpass filter of 10 nm bandwidth centered at 527 nm. The scattered signal was collected perpendicular to the laser sheet. The visible laser sheet at 527 nm was formed from a dual-cavity, frequency-doubled pulsed Nd:YLF laser beam (Dual Darwin 527-80M, 21 mJ/pulse at 10 kHz, 180 ns pulse width). The Gaussian laser beam was shaped into a laser sheet

(L=100 mm, H=89 mm and w=1.2 mm) with a set of lenses consisting of a cylindrical negative lens, two spherical lenses and a positive cylindrical lens. LII and flame emission were recorded perpendicular to the IR excitation plane with a third PIMAX4 1024f intensified camera equipped with Sigma 105 mm (F2.8) lenses. A narrow bandpass filter with a bandwidth of 10 nm, centered at 450 nm, collected the transmitted light signal through a second dichroic mirror. LII signal and flame emission were recorded during 50 ns GW in prompt detection at a frequency of 3.33 Hz. A fourth PIMAX2 intensified camera equipped with Sigma 23-300 mm (f/3.5-6.3) lenses collected the flame emission 80 ns before the LII signal during a GW of 50 ns. This camera recorded the images at 3.33 Hz and was synchronized with the PIMAX4. A narrow bandpass filter with a bandwidth of 10 nm, centered at 580 nm, collected the reflected light signal. The corresponding LII laser beam (1064 nm, 9 ns pulse width, 10 Hz, Litron 850G) was shaped into a homogeneous laser sheet (L=100 mm, H=89 mm and w=0.4 mm) with a negative cylindrical lens and two positive cylindrical lenses. The laser fluence at the focus point is 0.25 J/cm^2. This fluence value is superior to the LII sublimation threshold of ~0.18 J/cm^2 for mature soot and was chosen to compensate for the attenuation of the laser beam while passing through the dense pressurized sampling volume. All four cameras were flat field corrected, and their focal point was adjusted with a calibrated target before each measurement. After the stabilization of each OC, a total of 10 minutes were dedicated to record images with the coupled optical system. The two high-speed cameras for OH* and scattering were used to recording 15000 images each at 10 kHz simultaneously, followed by the record of the flame emission and LII plus flame emission at 3.33 Hz with 80 ns delay between the intensified cameras. Each PIMAX camera recorded a series of 1500 images. A correction factor was calculated for the flame emission recorded with the PIMAX2 camera to subtract from images recorded with the PIMAX4 camera. This correction factor was estimated while measuring the flame emission with the two cameras without inducing LII signal and flat field measurements.

Numerical methods

The simulations presented hereinafter were performed using the AVBP solver developed by CERFACS [6]. AVBP solves the fully compressible multi-species Navier-Stokes equations on unstructured grids. The considered computational domain is shown in Fig. 2, where it is pos-

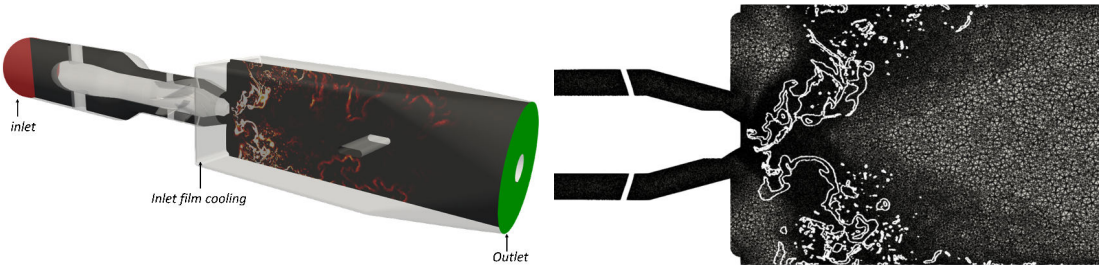

Figure 2. The computational domain used for LES of the MICADO test bench (left-hand side) and mesh obtained after mesh adaptation (right-hand side). The white iso-line represents an instantaneous iso-contour of heat release rate at $2\times10^9 \mathrm{W}/m^3$.

sible to distinguish the air inlet which feeds the swirler, the cooling films and the outlet. The boundary conditions were fixed to be consistent with Tab. 1 for the OC1. The Lax-Wendroff advection scheme, second-order in space and time, was employed for all calculations. An unstructured mesh counting 19M elements was initially generated, imposing a uniform sizing inside the swirler channel and the combustion chamber. A first reactive simulation run using this coarse mesh to then apply static mesh adaptation, similarly to [7]. Next, the zone to be refined was tagged based on the heat release rate field and the local sizing was adapted targeting a flame thickening factor for Dynamic Thickened Flame LES (DTFLES) of 30 in all the flame regions. This led to a mesh counting 57M elements mostly refined in the flame zone, used for all the calculations shown in the following.

The subgrid turbulent contributions were included thanks to the SIGMA model [8]. The DTFLES model [9] was used to describe the flame propagation, where the efficiency function is computed based on the formulation proposed in [10] with $\beta = 0.5$. The liquid phase was modeled with a Lagrangian approach. A standard set of modeling choices was selected for the air-fuel interactions, where the drag contribution was included in the equation for the momentum of the liquid phase with the hypothesis of a spherical shape, whereas the evaporation rate was computed based on the model of [11]. A standard correlation for pressure atomizers from [12] was applied to obtain a Sauter Mean Diamter (SMD) of 44 μm, used for a Rosin-Rammler distribution with a dispersion parameter q fixed to 2.5. As far as the chemical description is concerned, two sets of calculations were performed. First, a two-step globally reduced chemistry, derived in [13], was used to compute the main features of the flame and to draw the first comparison with the experimental data. This calculation is named in the following **2S-BFER**. Global chemistry, albeit able to accurately predict global flame quantities such as the laminar flame speed and the burnt gas state, does not provide an estimation of pollutants, such as soot precursors. Therefore, considering the goals of the present study, the Analytically Reduced Chemistry (ARC) scheme proposed in [14] was employed to predict both the flame structure and the gaseous soot precursors. This simulation with ARC started from the 2S-BFER solution. The ARC scheme counts 29 transported species and 15 species in a Quasi Steady State. After a first computational step to flush out the 2S-BFER initialization, the Lagrangian Soot Tracking (LST) model proposed in [14] was activated to compute soot levels. The LST method, developed by CERFACS, considers soot particles as point sources with their characteristic properties (e.g., temperature, size, velocity). Soot particles are considered spherical at the nucleation stage, then their surface evolves depending on their history (collisions, surface reactions). The reader is referred to [15] for a complete description of the LST approach. This calculation is named in the following **ARC-LST**. It should be pointed out that, during the flush-out of this computation from the 2S-BFER case it appeared that the ARC flame stabilisation tip was much more sensitive to the mesh resolution and thickening factor. Therefore, keeping the same parameters as in the 2S-BFER case led to a flame detachment from the injector. In order to avoid this, the thickening factor was fixed to one in the zone close to the injector. This adjustment represents a draft solution to focus our attention on soot production and to compare with the available experimental data. However, the problem of stabilizing flames in this configuration with a semi-detailed chemistry is still under investigation to understand and formulate an appropriate method.
For the investigated operating condition, it is considered the flame was stabilized in the first half of the combustion chamber. With this hypothesis, the Flow Through Time (FTT) was estimated to 5 ms. For the ARC-LST calculation, the flush-out was carried out over 3 FTTs and statistics were collected during more than 2 FTTs. As discussed during the description of the results, the flame shows a strong coupling with the liquid phase and consequent important dynamics. The averaging process is ongoing to obtain a more converged set of statistics, especially for soot.

Results

This section evaluates the formation of soot particles for Jet A-1 and ATJ through experimental and modeling tools. First, spray characterization, OH* chemiluminescence and LII signals are presented to identify the main parameters leading to soot formation for the three OC with Jet A-1 and ATJ fuels. Then, the comparison between experiments and LES is proposed, followed by an insight into the soot generation process obtained for OC1 and Jet A-1.

Experimental results

Spray vaporization and dynamics are inferred from instantaneous scattering images that are exhaustively described. Scattered light from multi-phase combustion is attributed to non-vaporized

fuel droplets (Mie scattering) or soot particles (Rayleigh scattering). In our application, Rayleigh scattering signals are inferior to Mie scattering due to different scattering cross-section values (µm for droplets and nm for particulates) and polarization properties. Hence, recorded signals must be pre-processed to assign them to various phases of matter in the combustor. From the totality of recorded images, two categories of signals were observed and based on their intensity values and sharpness, it is possible to differentiate between signals belonging to spray or particulates. In bright regions at the periphery of the spray were identified soot pockets trapped

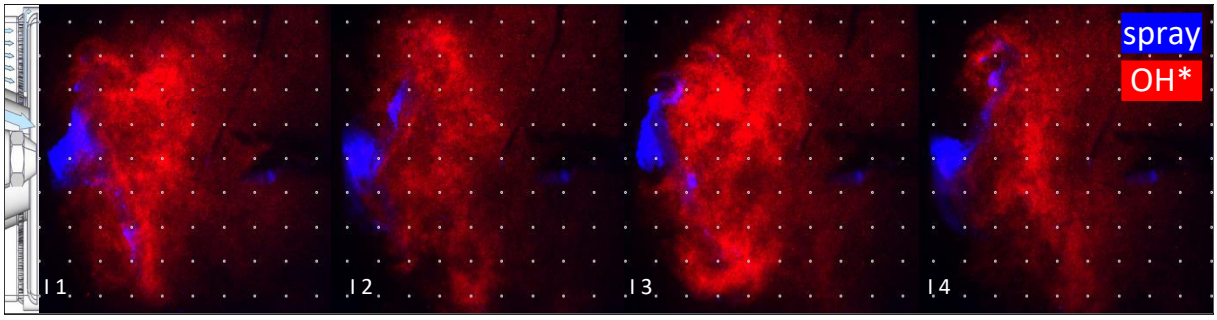

Figure 3. Overlay of instantaneous OH* (red color) and non-vaporized fuel (blue color) images for OC1 - Jet A-1 fuel. The dotted mesh has 10 mm distance between each neighboring dot. Images (I1-4) were randomly selected from the dataset.

between the spray scattered signal and the detector, similar to shadowgraphy. These dark regions were identified when soot was localized near the sampling focal point. Instantaneous scattering images are predominated by light scattered from the non-vaporized fuel, while light scattered from soot was identified for OC3 with Jet A-1 and ATJ fuels only. This separation is possible when particulates are not interfering with the non-vaporized fuel region, as well as in the case of high local soot concentrations on instantaneous images. Specific features are determined on the instantaneous images, which differentiate mainly the OC and less among the fuels. Similar patterns of the spray angle and coverage area are identified for OC1 and OC2, while OC3 spray shapes are notably different from the first two OCs due to the oscillation of the cone angle and penetration depth from one image to another. Several instantaneous images corresponding to OC1 - Jet A-1 fuel are shown in Fig. 3 (blue-colored area), where the coverage spray zone is compact near the injector and thinner towards the spray branches. Low and high-frequency oscillations of the spray are identified with the 10 kHz recording frequency. For OC1 and OC2, the spray is localized on a 10 mm narrow region next to the nozzle, followed by a ramified branch that expands between 10 to 20 mm from the combustor backplate. Thin droplets of the swirling spray extend from 25 to 45 mm and then impinge on the combustor walls. The spray shape varies considerably for the OC3 case, indicating that this condition is prone to instability. For OC3, the spray penetration depth oscillates between 20 and 45 mm, with a synchronous fan angle oscillating between 140° and 80°. Spray oscillations for each OC and fuel were determined after applying fast Fourier Transform (FFT) on summed scattered intensities of the entire frame for a series of 15000 images. The dominant frequency of Jet A-1 fuel in OC1 is 1044 Hz, 1188 Hz corresponds to OC2 and 232 Hz to OC3. Respecting the same OC order, ATJ fuel has the following dominant frequencies: 1043 Hz, 1197 Hz and 230 Hz. The three OCs have a frequency shift between Jet A-1 and AtJ fuel. This frequency shift is negative between Jet A-1 and ATJ for OC1 and OC3 and reversed for OC2, where higher frequencies are detected for AtJ fuel as against Jet A-1. After the FFT analysis, several prominent frequencies were identified for each OC, with four non-harmonic modes for OC1, two for OC2, and six harmonics for OC3. These modes correlate with the changing shape of the spray, its stability and mixing with surrounding hot gas. For instance, the reverse frequency shift between the two fuels in OC2 may be related to the global equivalence ratio's role in the vaporization process rather than the operating conditions. This fact is attributed to the fuel-to-air ratio (FAR), which is smaller for Jet A-1 than ATJ in OC2. FAR values of Jet A-1 in OC1 and OC3 are higher

than for ATJ. Identified frequencies can also be attributed to hydrodynamics or thermoacoustic oscillations. The discussion is oriented on averaged images of non-vaporized fuel, presented in Fig. 4. It has to be noted that the flame is slightly asymmetrical, and some regions of the visualization window were damaged or fouled during the experiment. We limit our discussion to the visible regions of the flame through the optical port view. It is also pointed out that on the images with the fields of averaged signals (Fig. 4, 5, and 6), lines and ticks for the simulated case are represented with claret color to highlight the experimental data used for comparison with the numerical method. Spray shape changes with the OC but not significantly with the fuel. On average, for OC1, the spray is localized near the injector (well-defined edges over 5 mm), followed by an opening of 45° until 45 mm, where the spray is impacting the walls. For the OC3 case, the spray extremities are not touching the walls due to the predominant spray coverage area on the central axis of the chamber and instability. The spray angle near the injector is slightly increasing from OC1 to OC3. At the same time, a slight broadening in the spray fan angle is observed between Jet A-1 and ATJ for the three cases, as referenced in Fig. 4, with green arrows. These changes can rely upon the physical properties of the fuel, and it may be an indicator of different vaporization processes from one fuel to another. Standard error deviation (Std) field images (not shown in the text) corresponding to averaged images, display a higher spread of ATJ scattered signals on the spray region as against the Jet A-1, suggesting again that the vaporization of the two fuels is diverse. Indeed highly scattered signals indicate a dense spray, while weakly scattered signals are typical of a more diluted spray. Overall, averaged intensities from the spray are higher next to the injector region for ATJ fuel in the three OC. Conversely, Jet A-1 spray branches are denser than ATJ cases.

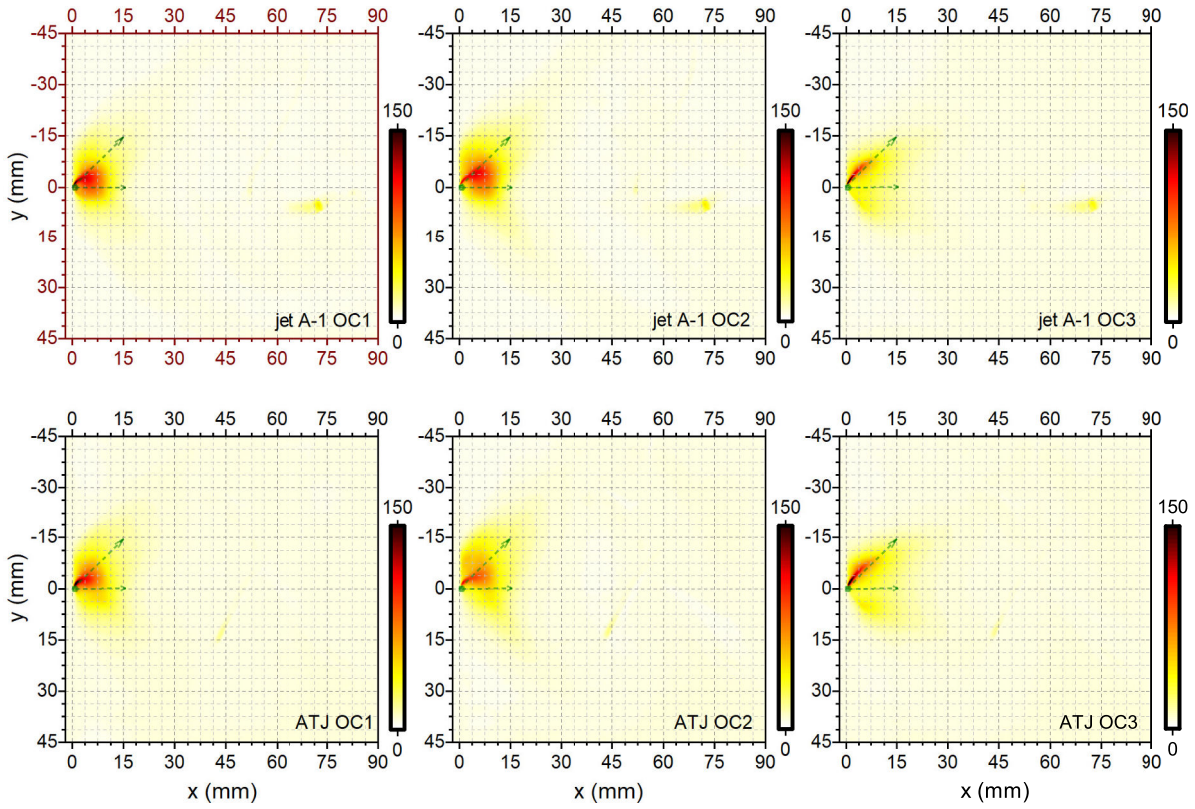

Figure 4. Average image fields with the scattered signal from non-vaporized fuel. Averaged images were obtained from a series of 2000 instantaneous images.

Simultaneous detection of OH* chemiluminescence and fuel scattering gives insight into flame-flow-spray interactions [16]. Hence, scattering data is compared with the heat release zones identified via the OH* chemiluminescence to understand fuel vaporization and fuel/air mixing.

In particular, OH* chemiluminescence is line-of-sight integrated and is used to infer the bulk dynamics of the flame structure. In addition, spray dynamics can be correlated with the OH* to determine a correlation factor between the vaporization of the fuel, mixing properties and the flame front. On instantaneous images, OH* signals are predominant at the periphery of the spray branches, following their oscillations and propagation. Previous works mentioned that higher OH* intensities are associated with the premixed part of the combustion since there is a higher production yield in these premixed regions of the fuel or next to the thin droplets [16]. Similar oscillation frequencies of the flame front, as the ones identified from scattering data, were obtained after the FFT analysis of the instantaneous image datasets. The magnitude of the frequency modes is higher for Jet A-1 fuel on the three OCs and the predominance of the modes did not change with respect to the frequency modes identified from fuel scattering. The order of the frequency shift between the non-harmonic and harmonic modes of the two fuels is also respected. Averaged emission OH* for the three cases and two fuels are presented in Fig. 5. Each OC is dominated by a corresponding flame front, which is not changing significantly among selected fuels, except for its magnitude. The heat release rate is expanding almost identically on the vertical axis for OC1 and OC2, and for OC3, the heat release is dominant in the inner recirculation zone of the flame. On the horizontal axis, the shift of OH* intensities from the injector toward the exhaust suggests that the flame is stabilized differently for the three OCs. For OC2 and OC1, the flame is stabilized closer to the injector, with a peak

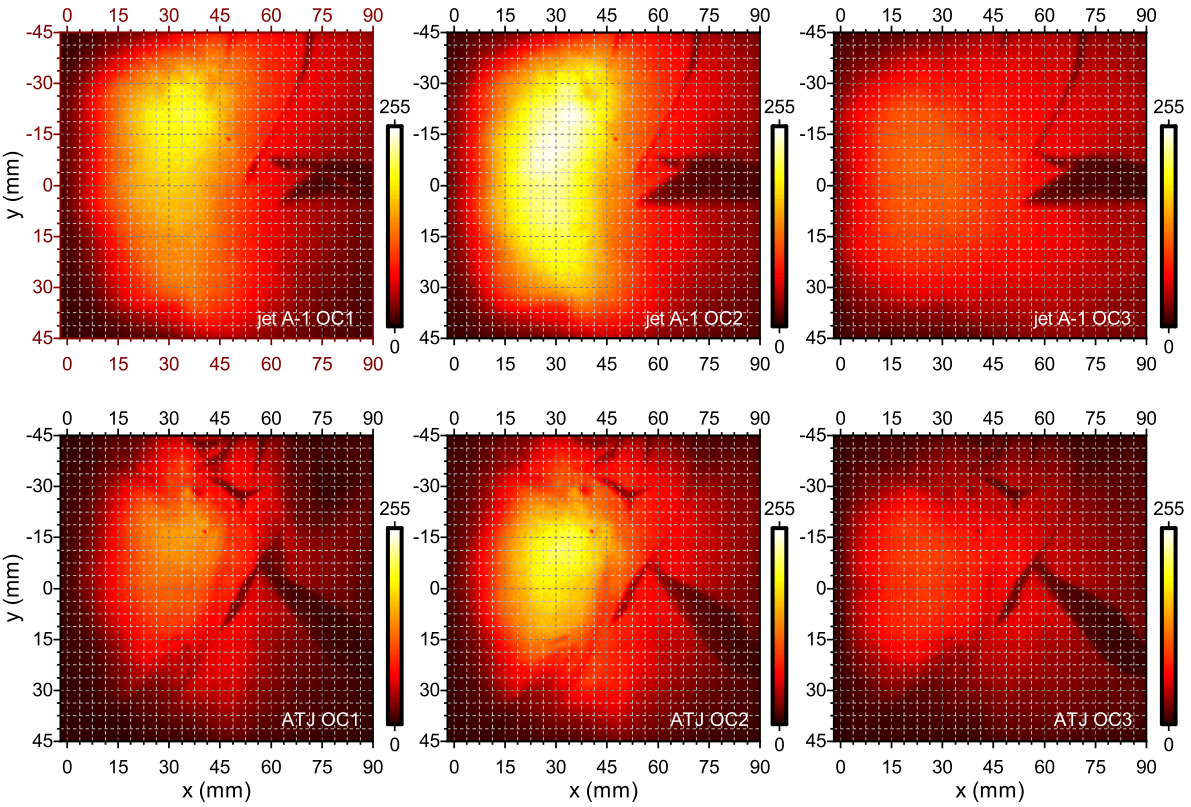

Figure 5. Average OH* chemiluminescence fields measured for the two fuels and three OCs. Averaged images were obtained from a series of 2000 instantaneous images.

of heat release near 30 mm, indicating a faster fuel evaporation rate and improved mixing. OC3 case is characterized by lower OH* intensities on the averaged image, with a stabilization peak between 15 and 30 mm and a higher turbulence rate since the Std is the highest among the three OCs, and it corresponds to the frequency mode at 244 Hz. Unexpectedly, Jet A-1 fuel combustion is characterized by a higher OH* emission than the one displayed by ATJ in the three OCs. A positive linear correlation exists between the FAR and OH* ratio of the two

fuels for OC1 and OC2, but this trend is changing for OC3, the unstable condition. Because the observed difference between the heat release of the two fuels cannot be explained by the fuel LHV only, it is suggested that the local mixing influences the heat release as well, which can affect the evaporation of fuel. It is suggested that differences in the local mixing, which result from the turbulence and the evaporation rate, directly affect the heat release rate and the concentration of soot precursors and soot particles. Soot particle regions were identified with the LII technique, which is highly sensitive (few ppb) for their detection. Average LII signals (flame emission subtracted) are displayed in Fig. 6. Spatially, soot averaged fields are shifted toward the exhaust from the OH* zones for OC1 and OC2. This trend is not kept for OC3, where soot particles are mainly detected in the same region as OH*, due to the highly turbulent behavior of the flame and instabilities. Similar spatial distribution characterizes OC1 and OC2, with reduced average soot volume fractions (few ppb). For these two cases, soot is present near the walls after 30 mm from the combustor back plate. An outer corner recirculation zone (CRZ) is observed near the back plate region, mostly for OC1 and less prominent for OC2. The probability of soot detection on instantaneous images is low (high Std) for the first two cases.

Soot filaments and pockets with high intensity (tens of ppb) are identified for OC1. A few in-

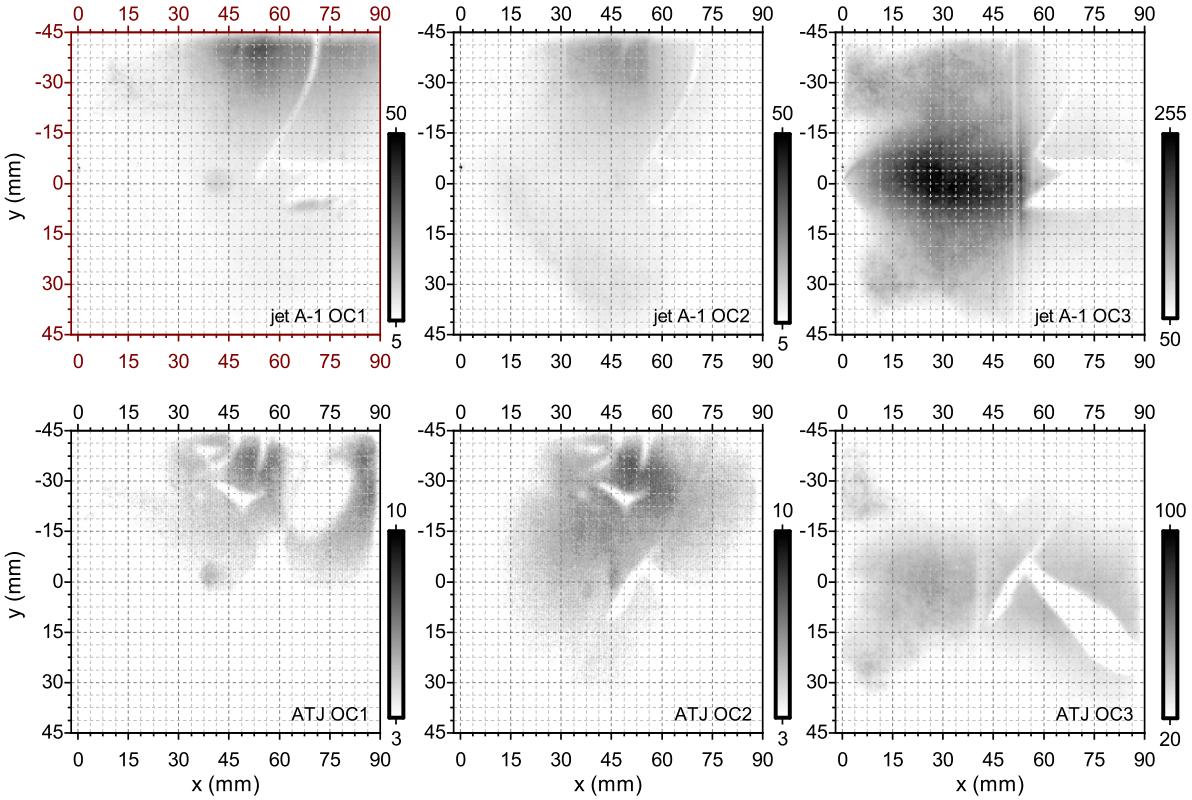

Figure 6. Average LII signal detected for the three OCs and two selected fuels. Averaged images were obtained from a series of 1500 instantaneous images.

stantaneous images corresponding to OC1 - Jet A-1 are shown in Fig. 7. Soot zones identified in OC1 for Jet A-1 have well-defined wrinkled structures, while for the same OC and ATJ fuel, it is only possible to detect some soot patches with low LII signal representing a few percent only from the total of the signal detected for Jet A-1 fuel. LII signals are at their detection limit for ATJ cases 1 and 2. The CRZ is not well delimited in the OC2 (high Std) case because the probability of identifying a soot filament in this region is low. The formation of soot is particularly interesting for OC3. High values (ppm) of LII signals are identified on the instantaneous images, where soot coverage is similar to corrugated flamelets. In this case, soot is all over the combustor and, most of the instantaneous images are covered with soot in the inner recirculation zone (IRZ), the spray region and the CRZ near the back plate. The soot volume fraction is

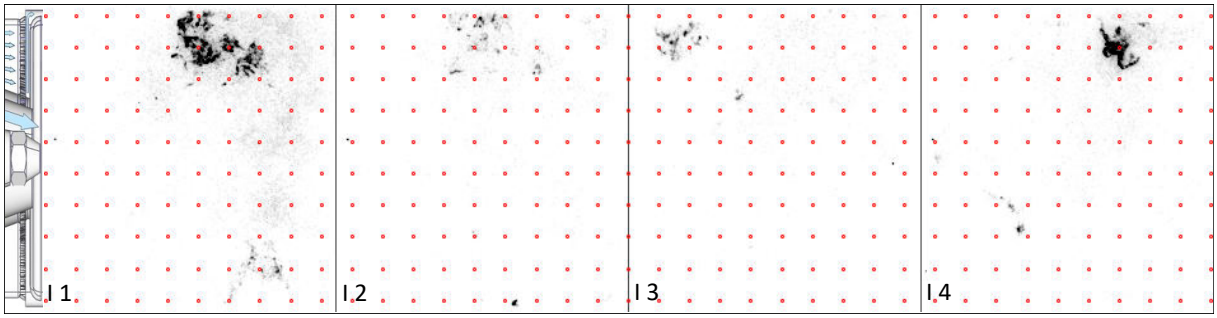

Figure 7. LII instantaneous images for Jet A-1 - OC1. Dotted scale corresponds to 10 mm distance. Images (I1-4) were randomly selected from the dataset.

estimated to be a few ppm on the averaged images. ATJ fuel produces three times fewer soot particles for this OC. The high predominant sooting behavior of OC3 was also captured with the scattering techniques, where soot is mainly identified in the IRZ toward the exhaust when the spray is broader and closer to the back plate. High residence time is identified for soot when the spray has a large fan angle (140°) and is localized near the injector; in this case, soot structures persist in the chamber for a few µs until the penetration depth of the spray increases and displaces the soot zones toward the combustor walls. The movement can be associated with low-frequency spray dynamics. High soot formation rates are associated with regions with high equivalence ratios since the fuel is not completely evaporated - data backed up by Mie scattering where the density of the fuel is higher than the other instantaneous images.

Comparison between experimental and LES results

This section analyses the numerical data obtained with Jet A-1 fuel on the OC1. The aim is to assess the capabilities of the selected numerical setup in reproducing the main characteristics of the flame and to provide a better understanding of the soot generation in the considered case. Fig. 8 shows a summary of the instantaneous (top-half) and time-averaged (bottom-half) fields for velocity, temperature, heat release rate and evaporation rate. The chosen view corresponds to the experimental window, where the fresh air duct has been included for clarity. A swirling flow field is generated with the creation of an IRZ, highlighted with the white iso-line at zero axial velocity, which brings burnt gases towards the injector. The flow field is also characterized by the presence of CRZ generated by the shear between the main swirling flow field and the cooling films. The flame is stabilized at the shear layer between the burnt gases in the IRZ and the fresh air coming from the swirler with a resulting V-shape. This zone corresponds to the location of the stoichiometric lines shown on the temperature and heat release rate contour plots. An important part of the flame heat release rate is also located in the near wall zone. The flame stabilization process is explained as follows: once injected, part of the spray almost immediately evaporates and generates a region with high values of equivalence ratio in the near injection zone. This creates the conditions to stabilize the inner flame branch in the shear layer between the burnt gases and the fresh air. Another part of the spray is instead able to pass this region and evaporates further downstream, i.e., near the chamber walls. This generates the second part of the flame in the shear layer between the fresh air and the CRZ. This explanation is supported by the evolution of the liquid phase evaporation source term shown in Fig. 8(d). Both the instantaneous and time-averaged evolutions of the liquid phase mass transfer are reported. Looking in particular at the time-averaged result, it is evident that the flame extends over the same region where the spray evaporates. This finding suggests an important coupling between the liquid phase and the flame in the present case.

In order to compare the LES results with the experimental data provided in the previous section, Fig. 9 reports the time-averaged line integrated heat release rate and liquid volume fraction over the experimental window. The flame seems located coherently with the experimental find-

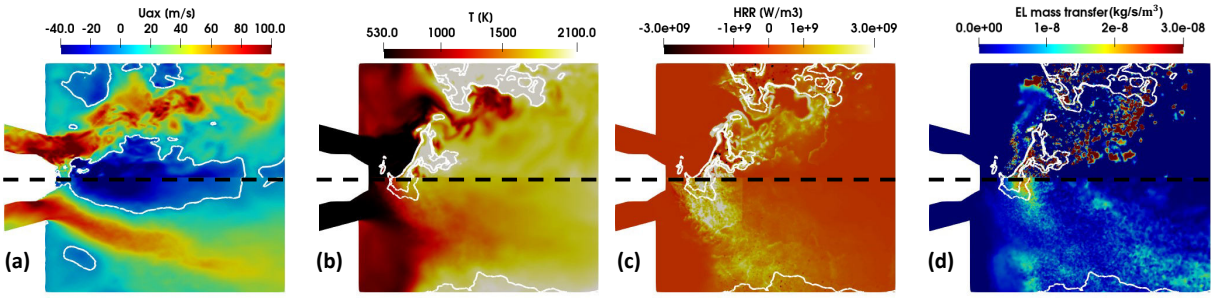

Figure 8. Instantaneous (top-half) and time-averaged (bottom-half) distributions of (a) axial velocity, (b) gaseous temperature, (c) flame heat release rate and (d) liquid evaporation rate over the chamber mid-plane for the ARC-LST case. The white line on the axial velocity plot represents the iso-contour at $u_{ax} = 0m/s$, while on the other three figures it shows the zone with a gaseous equivalence ratio $0.8 \leq \phi_g \leq 1.1$.

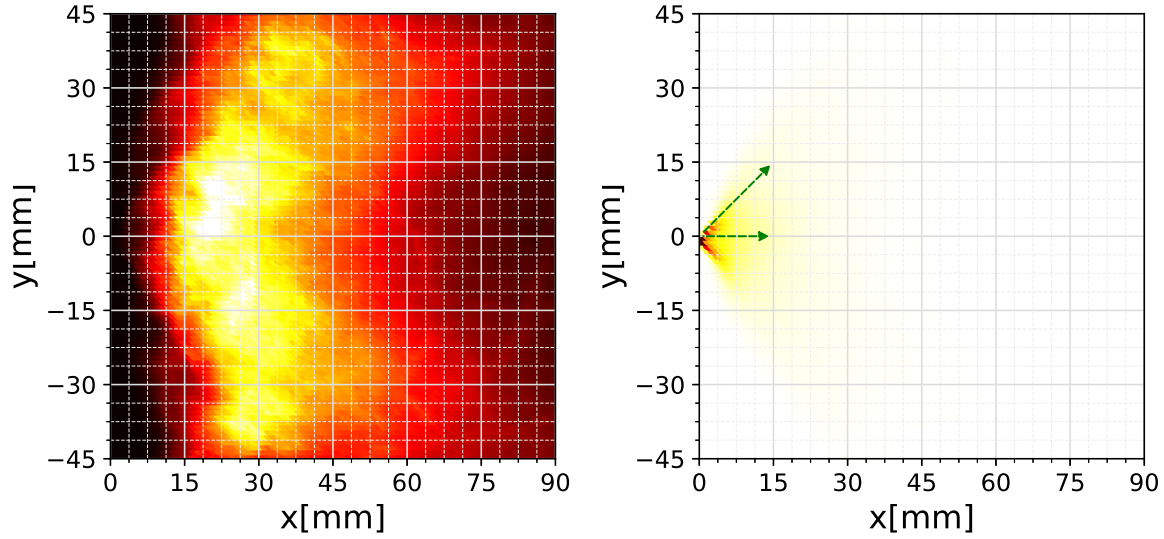

Figure 9. Line integral of the heat release rate (left-hand side) and of the liquid volume fraction (right-hand side) obtained from the ARC-LST case.

ings shown in Fig. 5 with a peak of heat release around the combustor centerline and a wide extension in the axial and radial directions. The spray looks also consistent with Fig. 4 with an opening angle of around 45° and an axial penetration around 15 mm (see the green arrows in Fig. 9). Therefore, from a qualitative point of view, the proposed numerical setup seems capable of retrieving the macroscopic flame behavior. Hence, the attention is now directed toward soot prediction.

Fig. 10 reports on the left-side the instantaneous distribution of the soot volume fraction (f_v) combined with the naphthalene mass fraction. The spray trajectory is also displayed with blue points. The whole height of the combustion chamber is here reported (i.e. $50 \leq y[mm] \leq 50$) with respect to Fig. 6 (i.e. $45 \leq y[mm] \leq 45$). Additionally, the O2 and OH mass fractions are shown in the center of Fig. 10, together with the soot source terms on the right-side. The source terms do not account here for nucleation and only contain oxidation on top-half and surface growth plus condensation on the bottom-half. Looking at the distribution of soot source terms, a clear correlation with the naphthalene appears: in the near injection zone and at the wall, $C_{10}H_8$ is present, thus enabling the soot nucleation. The soot tends then to be partially oxidized by the oxygen, present in the IRZ, and by the OH near the combustor walls. In that zone, fresh oxygen is also injected at the cooling slots, thus generating a further soot oxidation region. All in all, this leads to an instantaneous soot distribution with two peaks, i.e., the first one in the near injection zone and the second near the walls, similar to what is reported experimentally.

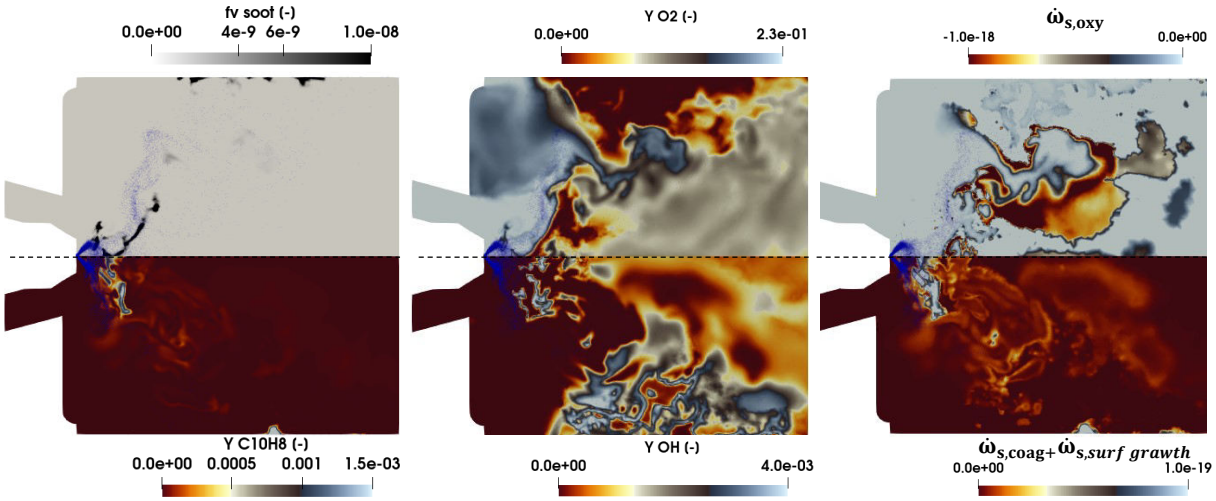

Figure 10. Instantaneous soot volume fraction combined with the naphthalene mass fraction (left-hand side), mass fraction of oxygen and OH (center) and soot evolution source terms (right-hand side) from the ARC-LST case. The soot source terms are expressed in $[kg/s/m^3]$ as units.

Nevertheless, considering the intermittency in the soot generation and the complex flame stabilization process pointed out for this operating condition, a much longer averaging time is required on soot and on the flame structure to reinforce such results and draw a more quantitative conclusion.

Conclusions

The sooting behavior of ATJ was experimentally investigated against Jet A-1 for three operating conditions (OC). It is shown that for similar FAR values, for the three selected OCs, ATJ fuel produces way fewer soot particles than Jet A-1. However, the sooting capacity of ATJ is not linear with the chamber pressure or the FAR. The various parameters that affect the formation of soot particles are the vaporization of fuel, which is different from one fuel to another, although the zones covered by the spray are similar in the two cases, the oxidation and heat release regions and the physical parameters of the fuel. In addition, flame instabilities can affect the production of soot, as observed for OC3, due to unfavorable mixing properties at the shear layer between non-vaporized fuel and surrounding hot gas. For this case, soot values were high for both fuels, but ATJ produced three times less soot and this fact can be related to both the chemical properties of the fuel and hydrodynamic conditions in the combustor. For OC1 and OC2, averaged soot values were near the detection limit (few ppb) for ATJ; conversely, instantaneous images are characterized by localized soot flamelets and pockets with high intensities of soot signals (tens of ppb). A further processing of instantaneous images with advanced statistical tools is envisaged in the future for a better understanding of the processes governing the formation of soot and differences induced by the ATJ and Jet A-1 on small temporal scales. In parallel to experimental findings, a numerical study based on LES was also proposed to characterize the case OC1 with Jet A-1 as a first step. The developed model seems able to capture the macroscopic characteristics of the spray and the flame regions. Similarly to experiments, soot regions are identified near the injector and close to the walls. A longer averaging time is undoubtedly required to draw quantitative conclusions on soot distribution and flame stabilization, which will be pursued in the near future. The present case presents a complex stabilization process with semi-detailed chemistry. As a consequence, an appropriate modeling strategy with respect to the one employed in the present study for this problem is currently under investigation. Ultimately, the model will be extended to multi-component formulation in order to account for SAF composition and directly compare it with the experimental data available with ATJ.

Acknowledgements
This project has received funding from the European Union Horizon 2020 research and innovation program under the Marie Sklodowska-Curie grant agreement No. 875538 in the project ALTERNATE and the ONERA internal research program PR CARBON. This work was granted access to the HPC/AI resources of TGCC under the allocations 2021-A0102B12504 and 2022-A0122B13460.

References

[1] ICAO.
URL http://www.icao.int/Pages/default.aspx

[2] A. Giusti, E. Mastorakos, Turbulent Combustion Modelling and Experiments: Recent Trends and Developments, Flow, Turbulence and Combustion 103 (4) (2019) 847–869. doi:10.1007/s10494-019-00072-6.

[3] A. Dreizler, H. Pitsch, V. Scherer, C. Schulz, J. Janicka, The role of combustion science and technology in low and zero impact energy transformation processes, Applications in Energy and Combustion Science 7 (2021) 100040. doi:10.1016/J.JAECS.2021.100040.

[4] Alternate Project.
URL https://www.alternateproject.com/

[5] A. Cochet, V. Bodoc, C. Brossard, O. Dessornes, C. Guin, R. Lecourt, M. Orain, A. Vincent-Randonnier, ONERA test Facilities for Combustion in Aero Gas Turbine Engines, and Associated Optical Diagnostics, AerospaceLab (11) (2016) 1–16.

[6] CERFACS AVBP website.
URL https://www.cerfacs.fr/avbp7x/

[7] P. Walter Agostinelli, Y. H. Kwah, S. Richard, G. Exilard, J. R. Dawson, L. Gicquel, T. Poinsot, Numerical and experimental flame stabilization analysis in the new spinning combustion technology framework, Proceedings of ASME Turbo Expo 2020 Paper No. GT2020-15035 (2020).

[8] F. Nicoud, H. B. Toda, O. Cabrit, S. Bose, J. Lee, Using singular values to build a subgrid-scale model for large eddy simulations, Physics of Fluids 23 (8) (2011) 085106.

[9] O. Colin, F. Ducros, D. Veynante, T. Poinsot, A thickened flame model for large eddy simulations of turbulent premixed combustion, Physics of Fluids 12 (7) (2000) 1843–1863.

[10] F. Charlette, C. Meneveau, D. Veynante, A power-law flame wrinkling model for les of premixed turbulent combustion part i: non-dynamic formulation and initial tests, Combustion and Flame 131 (1) (2002) 159–180.

[11] B. Abramzon, W. Sirignano, Droplet vaporization model for spray combustion calculations, International Journal of Heat and Mass Transfer 32 (9) (1989) 1605–1618.

[12] A. Lefebvre, Atomization and Sprays, 1988.

[13] B. Franzelli, E. Riber, M. Sanjosé, T. Poinsot, A two-step chemical scheme for kerosene–air premixed flames, Combustion and Flame 157 (7) (2010) 1364–1373.

[14] L. Gallen, A. Felden, E. Riber, B. Cuenot, Lagrangian tracking of soot particles in les of gas turbines, Proceedings of the Combustion Institute 37 (4) (2019) 5429–5436. doi:10.1016/j.proci.2018.06.013.

[15] L. Gallen, Prediction of soot particles in Gas Turbine Combustors using Large Eddy Simulation, Ph.D. thesis, Université de Toulouse (2020).

[16] S. Kheirkhah, J. D. Cirtwill, P. Saini, K. Venkatesan, A. M. Steinberg, Dynamics and mechanisms of pressure, heat release rate, and fuel spray coupling during intermittent thermoacoustic oscillations in a model aeronautical combustor at elevated pressure, Combustion and Flame 185 (2017) 319–334. doi:10.1016/j.combustflame.2017.07.017.
URL http://dx.doi.org/10.1016/j.combustflame.2017.07.017